3-D-Printed Dielectric Slab Rectangular Waveguide for TE$_{10}$ and TE$_{20}$ Mode Equalization

Germán Torregrosa-Penalva [ORCID], Héctor García-Martínez [ORCID], *Member, IEEE*, Paula Viudes-Pérez [ORCID], Enrique Bronchalo [ORCID], Ernesto Ávila-Navarro [ORCID], and Maurizio Bozzi [ORCID], *Fellow, IEEE*

Abstract— **The dielectric slab rectangular waveguide (DSRW) has been widely studied and used for increasing the single-mode bandwidth (BW) of rectangular waveguides. This work presents a DSRW for equalizing the group velocity of the first two propagating modes in the structure. Suitably scaled, this DSRW design can be used in chip-to-chip communications to yield interconnects that avoid dispersion while enhancing the BW density of these systems. A theoretical analysis is introduced to show the equalization BW attained depending on the slab dimensions with regard to the rectangular waveguide width and the dielectric permittivity of the materials that fill the waveguide. A proof of concept slab rectangular waveguide is designed to meet a 45% equalization BW around a center frequency of 10.0 GHz. The design is scalable and can be adapted to fit the dielectric permittivity of available materials. Several waveguide sections were fabricated using additive manufacturing (AM) techniques and two dielectric materials with different permittivities. Simulations and measurements confirm the waveguide behavior at the design frequency range. TE$_{10}$ and TE$_{20}$ modes exhibit the same group velocity of 0.36 × c_0 at 7.95 GHz.**

Index Terms— **Additive manufacturing (AM), chip-to-chip, dispersion, group velocity, interconnect, mode equalization, rectangular waveguide, slab waveguide.**

I. INTRODUCTION

THERE exists nowadays a rapidly growing demand of interchip communication capacity due to the intense data traffic associated with mobile and web applications, and machine learning workloads [1], [2], [3]. This has led to investigate the use of mm-wave and sub-THz frequency bands along with interconnect transmission media to guarantee reliable ultrahigh speed chip-to-chip communication links [4], [5], [6]. Implementations of chip-to-chip interconnects have

been devised by optical and electrical means. The main drawback of the optical approach is the difficulty to integrate the required elements in chip fabrication processes (like CMOS technology). In the electrical implementation case, several guiding technologies have been proposed: rectangular waveguide [7], dielectric waveguide [8], Si-filled rectangular waveguide [9], substrate-integrated waveguide (SIW) [10], and multimode (orthomode) waveguide [11]. Moreover, the main problems that limit the performance of these waveguides have been identified and are basically two: attenuation and dispersion [12], [13]. Dispersion in this context refers in particular to intramode dispersion since proposed communication interconnects are targeted as single-mode to avoid intermodal dispersion. However, higher transmission rates would be possible at frequencies above the cutoff frequency of the first higher order mode. This would enhance the so-called bandwidth (BW) density if intermodal dispersion is reduced to acceptable levels. Additionally, multimode SIW has been proposed for multichannel signaling systems [14]. The SIW structure in [14] can accommodate two orthogonal channels when the mode launchers are efficiently designed to prevent coupling between them. However, such a multimode SIW signaling channel has limited performance due to the fact that signals traveling in each mode propagate at different velocities. This could be solved if both modes in the SIW waveguide exhibited the same group velocity.

In this work we propose a simple approach for equalizing the first two modes propagating in a waveguide structure to guarantee the integrity of the propagating signals, when used above the single-mode BW to reach higher transmission rate interconnects. Recently, dispersion-equalization techniques have been proposed for SIW interconnects in the monomode regime at the expense of employing additional devices to the channel interconnect [15], [16]. To the best of our knowledge, our work presents for the first time a dielectric slab rectangular waveguide (DSRW) which is conceived and designed for obtaining equal group velocities for the first two modes propagating in the structure. This proposal would allow chip to chip communication links to work above the cut-off frequency of the first higher order mode in the waveguide optimizing the channel usage versus the occupied connection volume (with no use of additional or external elements). It consists in the usage of a DSRW as if it were a graded index optic fiber [17], [18]. In the optic fiber case, the dielectric permittivity profile in the structure is designed to

allow faster propagation velocities to those modes that travel larger distances [19], [20]. The DSRW can be employed to slow down the group velocity of the fundamental propagating mode at a given frequency while not affecting significantly the group velocity of the first higher order mode at the same frequency.

The DSRW was first conceived and has been employed since for increasing the single mode BW of rectangular waveguides Ayres et al. [21], [22]. However, the lack of available low loss dielectric materials with different dielectric permittivity values, and the difficulty to integrate them in conventional rectangular waveguide fabrication milling procedures has limited its use. In recent years, AM has become a technology mature enough to be considered for producing waveguide devices [23], [24]. It ensures fast and inexpensive prototyping of designed networks while allowing a variety of possibilities to the microwave circuit designer not accessible with traditionally unconnected technologies: waveguide, coaxial, or planar. AM facilitates the complete integration of these alternatives and provides a wide variety of techniques and materials to attain a particular implementation or response.

We present a proof of concept rectangular waveguide for equalizing the group velocities of the first two propagating modes in the structure in a 45% BW around the design frequency of 10.0 GHz for a $\pm 2.5\%$ group velocity deviation range. It consists of a DSRW fabricated using AM techniques and two dielectric materials with different permittivity values. The design is scalable and can be modified according to the frequency specifications and permittivity of available materials for applications such as chip-to-chip communications.

The work is organized as follows in six different sections. Section II gives the theoretical background necessary for designing a DSRW meeting a particular equalization bandwidth. Section III presents the particular proof of concept rectangular waveguide design, while Section IV provides a deep insight to the DSRW implementation and to the S-parameter characterization. Section V is devoted to the final results and the determination of the TE_{10} and TE_{20} group velocities. The work ends with the conclusions in Section VI.

II. DIELECTRIC SLAB RECTANGULAR WAVEGUIDE THEORY

The geometry of the DSRW is shown in Fig. 1. The rectangular waveguide is completely filled symmetrically with two dielectric nonmagnetic materials, one placed in the central portion of the waveguide and the other on the sides.

A comprehensive study of the longitudinal section electric fields in the structure is given in Ayres et al. [21]. The geometry of Fig. 1 imposes boundary conditions that imply that electric fields not presenting a y dependence are in fact TE modes. In Ayres et al. [21], expressions are given for determining the propagation constant and the electric field distribution of TE_{m0} modes with m odd for an empty rectangular waveguide loaded in its central portion with a dielectric slab (i.e., $\varepsilon_{rd} = 1$). Next, equations from Ayres et al. [21] are generalized for different values of ε_{rd} and also the electric field distribution of TE_{m0} modes with m even is given.
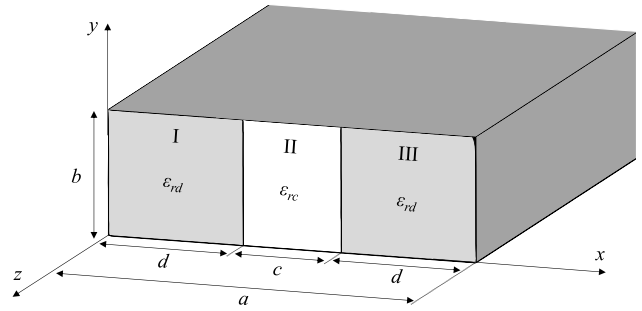

Fig. 1. Cross-section view of the DSRW. Metallic walls are shown in dark gray color, the high permittivity region in white color, and the low permittivity region in light gray.

The transversal electric field distribution for TE_{m0} modes in geometry of Fig. 1 is given by

$$E_y = j\omega\mu_0 \frac{\partial H_z}{\partial x} \cdot \begin{cases} \left(\frac{d}{p}\right)^2 & \text{in I and III} \\ \left(\frac{s}{q}\right)^2 & \text{in II} \end{cases} \tag{1}$$

where

$$H_z = H_0 g(x) e^{j(\omega t - \beta z)}$$

$$\left(\frac{p}{d}\right)^2 = \varepsilon_{rd} k^2 - \beta^2, \text{ and} \tag{2a}$$

$$\left(\frac{q}{s}\right)^2 = \varepsilon_{rc} k^2 - \beta^2. \tag{2b}$$

H_0 being an arbitrary magnetic field amplitude, $s = \frac{c}{2}$, $k = \frac{\omega}{c_0}$, c_0 the speed of light in vacuum, and p and q frequency-dependent parameters determined by the boundary conditions

For m odd

$$g(x) = \begin{cases} \cos\frac{p}{d}x, & \text{in I} \\ \frac{\cos p}{\sin q} \sin\left(\frac{q}{s}\left(\frac{a}{2} - x\right)\right), & \text{in II} \\ -\cos\frac{p}{d}(a - x), & \text{in III} \end{cases}$$

and

$$\frac{\tan p}{p} = \frac{s}{d}\frac{\cot q}{q}. \tag{3}$$

For m even

$$g(x) = \begin{cases} \cos\frac{p}{d}x, & \text{in I} \\ \frac{\cos p}{\cos q} \cos\left(\frac{q}{s}\left(\frac{a}{2} - x\right)\right), & \text{in II} \\ \cos\frac{p}{d}(a - x), & \text{in III} \end{cases}$$

and

$$\frac{\tan p}{p} = -\frac{s}{d}\frac{\tan q}{q}. \tag{4}$$

The cutoff frequencies are obtained imposing $\beta = 0$ in (2a) and (2b) and substituting in (3) for the odd modes or in (4) for the even modes. Using (1), it is possible to calculate the transversal electric field distribution for TE_{m0} modes in the structure of Fig. 1. Meanwhile, equations (2a–b), along

with (3) for odd or (4) for even index m, can be solved for each frequency to obtain the dispersion diagram of the TE_{m0} modes in the structure of Fig. 1 as a function of the dimensions a and c, and the permittivities ε_{rd} and ε_{rc}. This leads to the following transcendental equation for the TE_{10} mode

$$\sqrt{k_c^2 - \beta_{10}^2} \cdot \tan\left[\left(\frac{a-c}{2}\right)\sqrt{k_d^2 - \beta_{10}^2}\right]$$
$$= \sqrt{k_d^2 - \beta_{10}^2} \cdot \cot\left[\frac{c}{2}\sqrt{k_c^2 - \beta_{10}^2}\right] \qquad (5a)$$

where $k_d = \omega \varepsilon_{rd}^{1/2}/c_0$ and $k_c = \omega \varepsilon_{rc}^{1/2}/c_0$. Analogously, for the TE_{20} mode,

$$\sqrt{k_c^2 - \beta_{20}^2} \cdot \tan\left[\left(\frac{a-c}{2}\right)\sqrt{k_d^2 - \beta_{20}^2}\right]$$
$$= -\sqrt{k_d^2 - \beta_{20}^2} \cdot \tan\left[\frac{c}{2}\sqrt{k_c^2 - \beta_{20}^2}\right]. \qquad (5b)$$

The solutions of (5a) and (5b), which have to found by numerical means, yield the dispersion relations $\beta = \beta_{10}(\omega)$ and $\beta = \beta_{20}(\omega)$. After numerical derivation, the group velocities $v_{g10}(\omega) = (d\beta_{10}/d\omega)^{-1}$ and $v_{g20}(\omega) = (d\beta_{20}/d\omega)^{-1}$ are obtained. Although not made explicit to simplify the notation, these velocities depend on a, c, ε_{rd}, and ε_{rc}. The absolute difference in group velocities between both modes can then be calculated as a function of frequency and design parameters:

$$|v_{g10} - v_{g20}| = F(\omega; a, c, \varepsilon_{rd}, \varepsilon_{rc}).$$

The design parameters a, c, ε_{rd}, and ε_{rc} can be varied within the ranges restricted by geometrical constraints or material availability to keep the function F under a prescribed tolerance ΔF in a given frequency band (f_1, f_2).

Fig. 2(a)–(o) shows the dispersion diagram and the group velocity of the first four modes (TE_{10}, TE_{20}, TE_{30}, and TE_{40}) which propagate in a DSRW with $a = 30.0$ mm and $b = 0.70$ mm. The DSRW is formed by two materials with $\varepsilon_{rd} = 3.0$ and $\varepsilon_{rc} = 7.4$. Also, shown are the normalized transversal electric field distributions obtained from (1) for the modes which propagate at 7.95 GHz. These characteristics are depicted for different values of the central portion width c, which is drawn in gray in the right column of set of Fig. 2. Fig. 2(b) and (c) indicates that the fundamental mode is strongly affected by a $c = 1.0$ mm thin layer of dielectric with $\varepsilon_{rc} = 7.4$. The sinusoidal field distribution of the homogeneous case becomes a close to triangular distribution while the group velocity of the TE_{10} mode equals that of the TE_{20} mode at 11.7 GHz. For this central slab width, only two modes propagate at 7.95 GHz. When $c = 7.0$ mm, Fig. 2(h) and (i) stresses that the TE_{20} mode behavior is significantly modified. For this case, there are two frequencies, 7.62 GHz and 13.43 GHz, where the group velocities of the TE_{10} and TE_{20} modes are equal. Fig. 2(k) highlights that the group velocity v_g of the TE_{20} mode is within $\pm 2.5\%$ of v_g of the TE_{10} mode in a BW ranging from 7.5 to 12.0 GHz. This is obtained when the central slab is $c = 8.0$ mm. At the particular frequency of 7.95 GHz, both group velocities equal $0.36 \times c_0$. Finally in Fig. 2(n), for $c = 9.0$ mm, it is possible to observe that there is no frequency where the group velocities of the first

two modes propagating are equal. It is also worth noting at the sight of Fig. 2(k) and 2(n) that for an intermediate value of c between 8.0 mm and 9.0 mm, it would be possible to equalize the group velocity of the first three modes propagating in the structure near 10.0 GHz.

From this analysis, it can be concluded that the DSRW studied can be used to obtain a wide BW where equalization ($\pm 2.5\%$ of v_g) of the TE_{10} and TE_{20} modes is met. While this result has a general value, the optimal dimensions can change if different values of the permittivity are adopted for the two dielectric materials. Additionally, even better results could be achieved by using a properly designed smooth transition between the two materials, instead of the sharp transition adopted in this work and shown in Fig. 1. For a practical chip to chip communication link implementation, material permittivities available in chip fabrication processes (like CMOS technology) should be considered. Also, the dimensions of the proposed DSRW waveguide should be scaled according to the targeted transmission frequencies.

Recently, equalization methods have been used for SIW interconnects in the context of intramodal dispersion [15], employing additional external passive devices and classical schemes. On the other hand, dispersion-free designs have been demonstrated for dielectric waveguides [25], where minimal dispersion can be achieved in multimode regime (along with higher data rates). In our DSRW design, intramodal dispersion is minimized by using frequencies well above the single-mode BW (ensuring higher data rates), while equalizing the group velocity of higher order propagating modes, thus minimizing the intermodal dispersion as well.

III. DESIGN FOR EXPERIMENTAL VALIDATION OF THE DSRW

In order to validate the expected behavior of the proposed DSRW, the following experiment was designed and simulated. Two DSRW sections with lengths $l_1 = 4.0$ cm and $l_2 = 7.0$ cm, were employed to determine the group velocity in the structure. The dimensions of the DSRW are $a = 30.0$ mm, $b = 0.70$ mm, and $c = 8.0$ mm, (with $\varepsilon_{rd} = 3.0$ and $\varepsilon_{rc} = 7.4$). S-parameters are used to obtain the group delay in each section, τ_{g1} and τ_{g2}. The group velocity is then calculated as

$$v_g = \frac{l_2 - l_1}{\tau_{g2} - \tau_{g1}} = \frac{l_2 - l_1}{\Delta \tau_g}. \qquad (6)$$

This procedure was applied to the TE_{10} and TE_{20} modes. At 7.95 GHz, both group velocities should be in agreement with those in Fig. 2(k) ($v_g = 0.36 \times c_0$). In order to demonstrate accurately the behavior of the proposed DSRW for equalizing the TE_{10} and TE_{20} modes, independent circuits with simple feeding networks were fabricated for each mode. However, both modes could be fed simultaneously as pointed out in recent works [14], [26].

A. DSRW for TE_{10} Propagation Design

Fig. 3 shows the two sections of different lengths employed to determine the group velocity of the TE_{10} mode in the
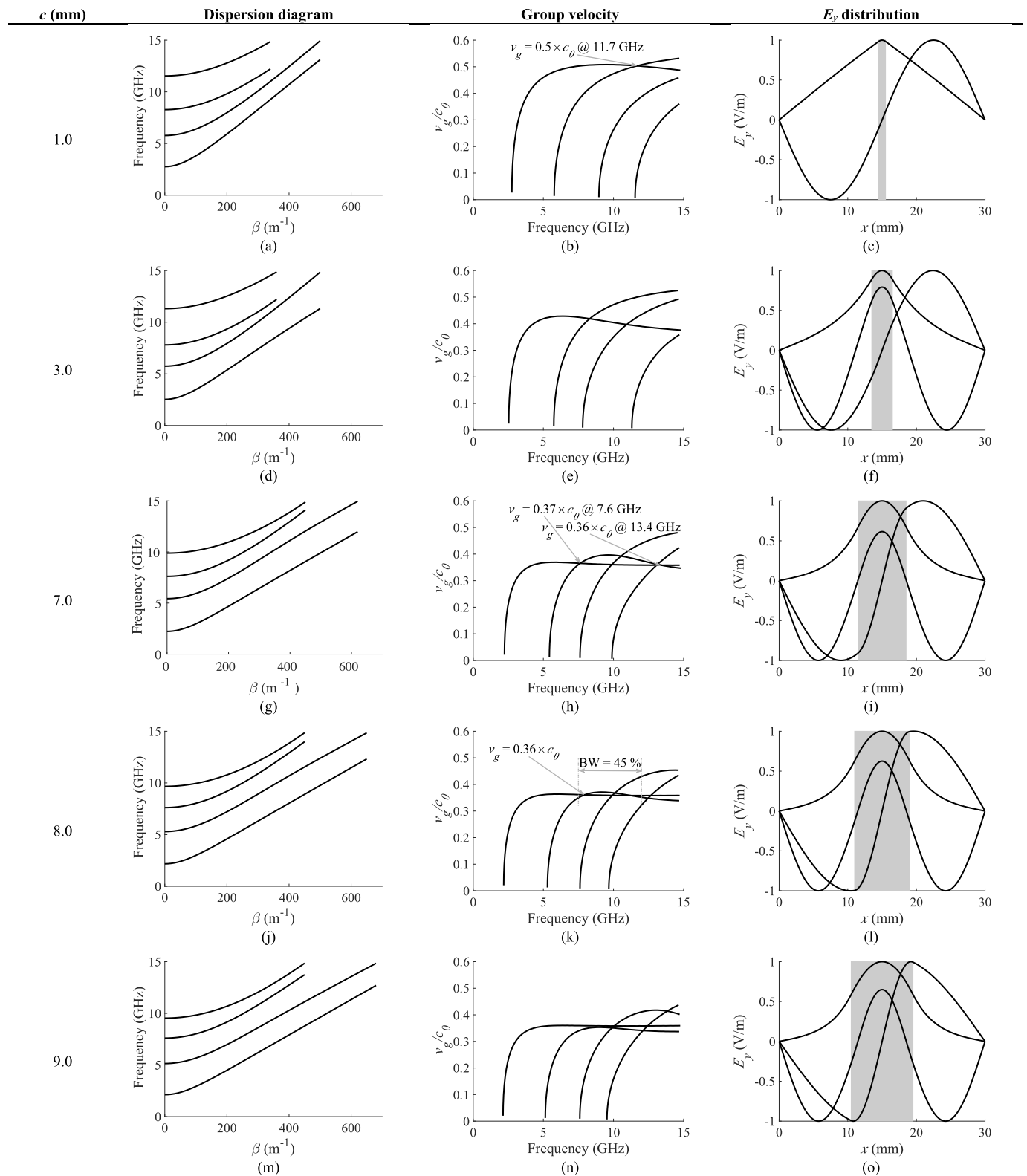
Fig. 2.   Dispersion diagram (left column) and group velocity (center column) of the first four modes propagating in the DSRW as a function of the central slab width c. Transversal electric field distribution of the first modes propagating at 7.95 GHz (right column), shown in gray the central slab width c.

DSRW structure using (6). The sections include microstrip to waveguide input/output transitions optimized to yield a good reflection coefficient response around 7.95 GHz. Microstrip to waveguide transitions are exactly the same for both DSRW sections of different lengths. The length of these transitions is 1.5 cm since our experimental measurement equipment limits the total length of devices under characterization to 10.0 cm. S-parameter simulations and optimization were carried
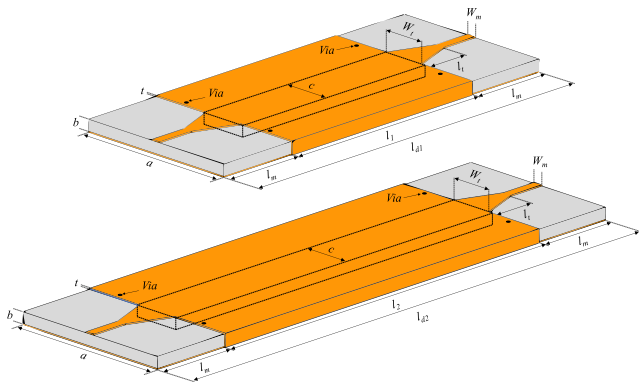
Fig. 3. DSRW views of the two sections of different lengths for TE_{10} mode propagation. Metallic parts are shown in orange. $\varepsilon_{rc} = 7.4$ region is shown in discontinuous line, the width of this region is $c = 8.0$ mm. The rest of the structure is formed by $\varepsilon_{rd} = 3.0$ material. The dimensions are (mm): $a = 30.0, b = 0.70, l_1 = 40.0, l_{d1} = 70.0, l_2 = 70.0, l_{d2} = 100.0, l_m = 15.0, W_t = 7.8, W_m = 1.73, l_t = 8.0$, and $t = 0.035$.

TABLE I

DIELECTRIC CHARACTERISTICS OF THE ADOPTED MATERIALS

Material	ε_r	$\tan \delta$
PREPERM 3D ABS dk 3.0	3.0	0.002
PREPERM 3D ABS dk 10.0	7.4	0.01

out using the commercial electromagnetic software Ansys HFSS.

The materials introduced in the simulation for implementing the DSRW sections are PREPERM 3-D ABS dk 3.0 for the low permittivity parts (ε_{rd}) and PREPERM 3-D ABS dk 10.0 for the high permittivity central part (ε_{rc}). Input/output 50 Ω characteristic impedance microstrip line to waveguide transitions are also synthesized on PREPERM 3-D ABS dk 3.0. A previous characterization [27] of these materials yielded the properties listed in Table I, which are included in the simulations.

DSRW sections in Fig. 3 include a couple of vias at each end to prevent the mode TE_{30} from being excited. These vias are located at the exact positions ($x = 5.74$ cm and $x = 24.27$ cm) where the TE_{30} mode transversal electric field exhibits its lateral maxima at 7.95 GHz according to Fig. 2(l). Their impact on the TE_{10} mode behavior can be neglected since the electric field magnitude for the fundamental mode at those positions is close to zero.

Simulated S-parameters for the 4 cm DSRW section of Fig. 3 are shown in Fig. 4. The matching transitions are optimized for 7.95 GHz. At this frequency, transmission losses are 1.0 dB while the reflection coefficient nears −30 dB.

Fig. 5 shows the simulated S-parameters for the 7 cm long DSRW section of Fig. 3. At 7.95 GHz, the $|S_{21}|$ parameter is − 1.7 dB while the reflection coefficient is well below −30 dB.

B. DSRW for TE_{20} Propagation Design

Fig. 6 shows the two different length sections used to determine the group velocity of the TE_{20} mode in the DSRW structure using (6). It should be noted that the 4 cm and 7 cm DSRW sections of Fig. 6 are identical to those of
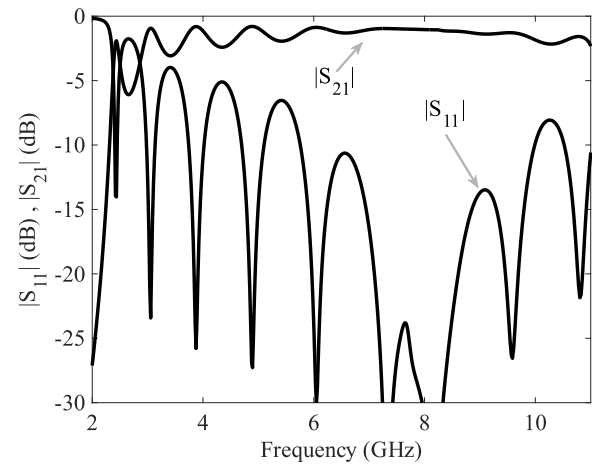

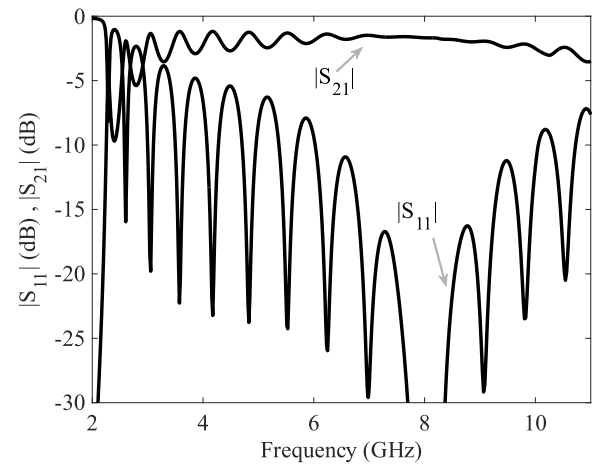Fig. 4. Simulated S-parameters for the DSRW with $l_1 = 4.0$ cm.

Fig. 5. Simulated S-parameters for the DSRW with $l_2 = 7.0$ cm.

Fig. 3. The only difference between both sets of waveguides is the input/output matching sections optimized for exciting the corresponding mode in the structure at 7.95 GHz. For the excitation of the TE_{20} mode in the DSRW, a T divider splits the signal in the input/output 50 Ω microstrip line into two 100 Ω microstrip lines [22]. Additionally, one of the paths includes an extra transmission line length to account for a 180° signal phase shift necessary to properly excite the TE_{20} mode. Both paths are fed to the DSRW at the exact positions ($x = 10.43$ cm and $x = 19.57$ cm) where the TE_{20} mode presents its transversal electric field maxima at 7.95 GHz, in agreement with Fig. 2(l). It should also be noted that the positions of these maxima are close to the position where the TE_{30} mode transversal electric field is very close to zero, [see Fig. 2(l)], preventing its appearance.

S-parameter simulations for the short and long DSRW sections shown in Fig. 6 are provided in Figs. 7 and 8, respectively.

The solution adopted for providing the extra 180° phase shift in one of the split paths for correct TE_{20} feeding, see Fig. 6, presents a reasonably narrowband behavior around the design frequency of 7.95 GHz. This means that the TE_{20} mode is being properly excited around that frequency, so
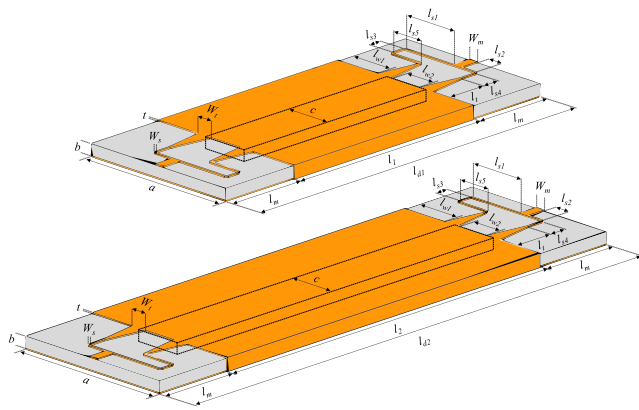
Fig. 6. DSRW views of the two sections of different lengths for TE_{20} mode propagation. Metallic parts are shown in orange. $\varepsilon_{rc} = 7.4$ region is shown in discontinuous line, the width of this region is $c = 8.0$ mm. The rest of the structure is formed by $\varepsilon_{rd} = 3.0$ material. The dimensions are (mm): $a = 30.0, b = 0.70, l_1 = 40.0, l_{d1} = 70.0, l_2 = 70.0, l_{d2} = 100.0, l_m = 15.0, l_{s1} = 10.63, l_{s2} = 3.34, l_{s3} = 2.60, l_{s4} = 3.27, l_{s5} = 6.39, l_{w1} = 8.86, l_{w2} = 6.42, W_t = 2.93, W_m = 1.73, W_s = 0.43, l_t = 7.80,$ and $t = 0.035$.
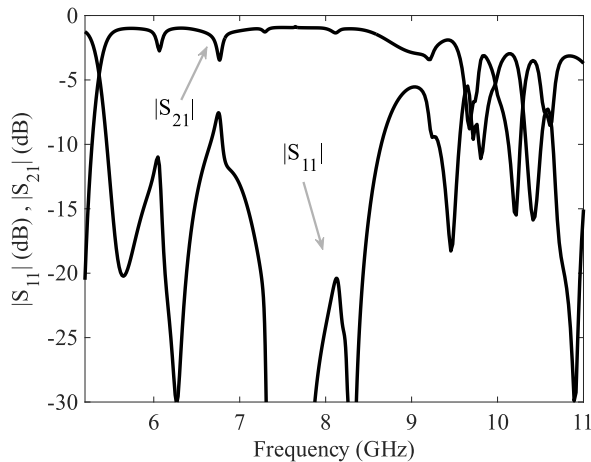
Fig. 7. Simulated S-parameters for the DSRW with $l_1 = 4.0$ cm.
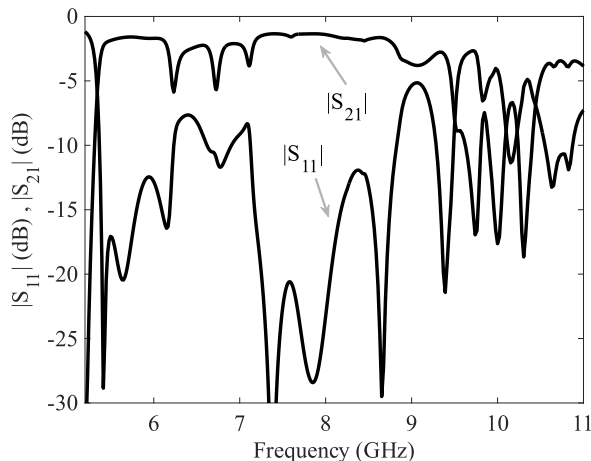
Fig. 8. Simulated S-parameters for the DSRW with $l_2 = 7.0$ cm.

S-parameter simulations are of interest around that frequency. At 7.95 GHz, the transmission and reflection coefficients for the 4.0 cm DSRW are, respectively, -0.97 and -26.0 dB
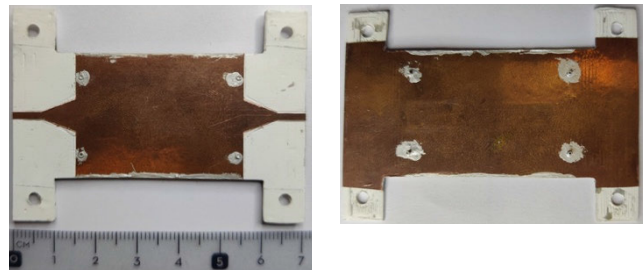

Fig. 9. Top and bottom views of the fabricated DSRW with $l_1 = 4.0$ cm for TE_{10} mode excitation.

(Fig. 7). For the 7.0 cm DSRW, these parameters are -1.37 dB and -25.8 dB (Fig. 8). In the case of the TE_{20} mode transmission in the DSRW, it should be mentioned that, in agreement with Fig. 2(j), the cut-off frequency is 5.34 GHz.

IV. DSRW FABRICATION AND S-PARAMETER MEASUREMENTS

The fabrication of the DSRW sections was carried out using a modified low-cost 3-D printer HTA3D Prusa i3 P3STEEL with a resolution of 0.015mm in the *XY* axes and a 0.4 mm diameter nozzle. The printer modifications consisted in the addition of a second extruder (Bondtech BMG-X2) so that the printer could handle simultaneously the printing materials described in Table I, and in incorporating a methacrylate isolating chamber for ambient temperature stabilization.

A metallization process followed the AM procedure. It consisted of gluing two 35 μm copper sheets (from basic copper) to both top and bottom faces of the DSRW. A thin layer of nonconductive epoxy glue 2216 B/A GRAY from 3M applied manually with a brush was employed. Finally, for a proper attachment, a hydraulic press was used to exercise a pressure of 150 N/cm^2 to the two copper sheets for one hour, with an ambient temperature of 24 °C and a humidity of 40%.

After the epoxy glue solidifies, a numerically controlled milling machine LPKF Protomat S42 was employed for producing the microstrip to DSRW transitions. Finally, a silver paint (Chemtronics) was applied with a brush to the lateral 0.7 mm high sides to properly enclose the waveguide structures.

Fig. 9 shows the top and bottom faces of the 4 cm long DSRW for excitation of the TE_{10} mode, and Fig. 10 shows the top view for the 7 cm case. As can be seen in the pictures, the implemented DSRW sections include the optimized transitions, the vias introduced to prevent the excitation of the TE_{30} mode and fiducial drills which allow a correct placement of the device during the milling process with regard to the $\varepsilon_{rc} = 7.4$ high permittivity region (not visible due to the copper sheets).

S-parameter measurements compared to simulations for both DSRW sections are shown in Figs. 11 and 12, for the short and long waveguide sections, respectively. Measurements were performed using Anritsu 3680 universal test fixture (which limits the maximum total length of devices under test to 10.0 cm). There is a good agreement between the responses. As expected, the optimum behavior is around the target frequency of 7.95 GHz. At that frequency, the measured

This article has been accepted for inclusion in a future issue of this journal. Content is final as presented, with the exception of pagination.

TORREGROSA-PENALVA et al.: 3-D-PRINTED DIELECTRIC SLAB RECTANGULAR WAVEGUIDE

7

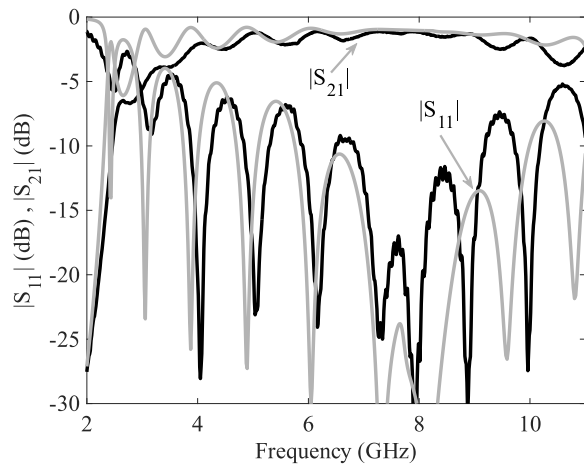Fig. 10.   Top view of the fabricated DSRW with $l_2 = 7.0$ cm for TE_{10} mode excitation.

Fig. 11.   DSRW with $l_1 = 4.0$ cm for TE_{10} mode excitation S-parameter measurements (black) and simulations (gray).
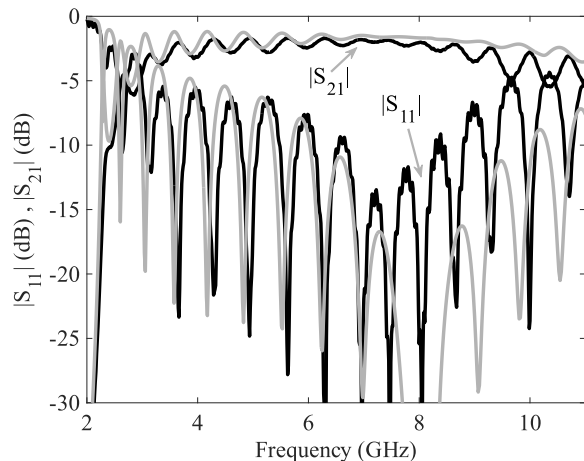

Fig. 12.   DSRW with $l_2 = 7.0$ cm for TE_{10} mode excitation S-parameter measurements (black) and simulations (gray).

Fig. 13.   Top and bottom views of the fabricated DSRW with $l_1 = 4.0$ cm for TE_{20} mode excitation.

Fig. 14.   Top view of the fabricated DSRW with $l_2 = 7.0$ cm for TE_{20} mode excitation.

Fig. 15.   DSRW with $l_1 = 4.0$ cm for TE_{20} mode excitation S-parameter measurements (black) and simulations (gray).

insertion losses are 0.1 dB higher than simulations for the 4 cm case and 0.4 dB higher for the 7 cm section. Meanwhile, the measured reflection coefficient at 7.95 GHz is under -30 dB for the 4 cm DSRW and -17.0 dB in the 7 cm case. This proof of concept DSRW presents measured insertion losses that might not be suitable for chip to chip communication applications. However, the AM materials and frequencies employed for demonstrating the equalizing capabilities of the proposed DSRW could be different in order to suit the needs of a practical chip-to-chip communication link.
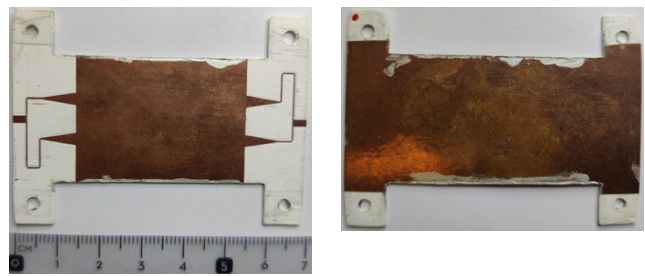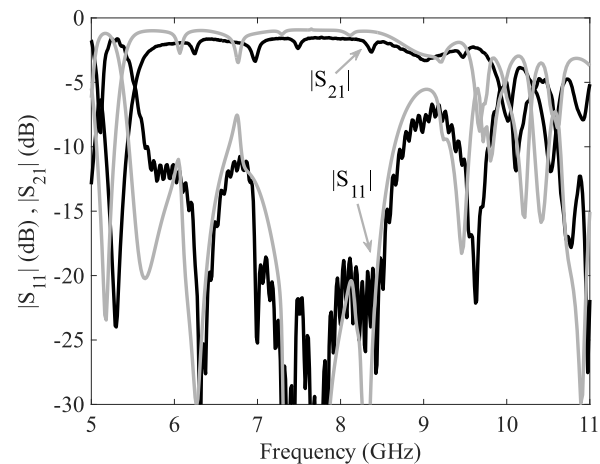
Figs. 13 and 14 show pictures of the fabricated DSRW structures for measuring the group velocity of the TE_{20} mode. These DSRW sections are identical to those in Figs. 9 and 10, except for the transitions to properly feed the required mode in each case.

Figs. 15 and 16 show the S-parameter measurements for the TE_{20} mode fed DSRW. They are compared to electromagnetic simulations presenting a good agreement between both sets of responses.

Simulations in Figs. 15 and 16 show that the TE_{20} cut-off frequency is 5.34 GHz while measured TE_{20} cut-off frequency results in 5.47 GHz. This implies a 2.0% error which could be attributed either to the AM fabrication process or to errors associated with the experimental measurement of the high $\varepsilon_{rc} = 7.4$ value. Also, characterization in Figs. 15 and 16 are of interest around 7.95 GHz due to the narrow BW nature of the TE_{20} feeding networks. At that target frequency, the
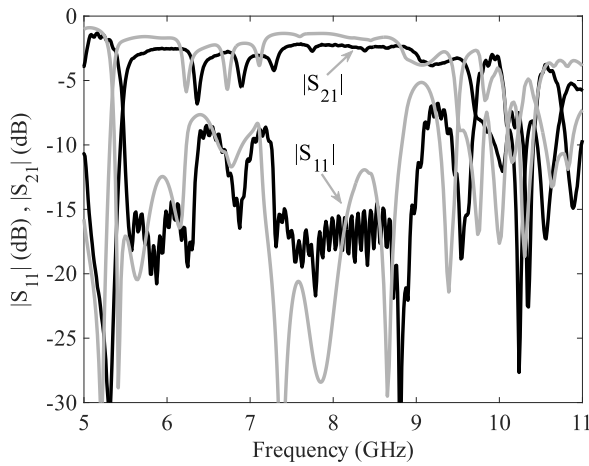
Fig. 16. DSRW with $l_2 = 7.0$ cm for TE_{20} mode excitation S-parameter measurements (black) and simulations (gray).
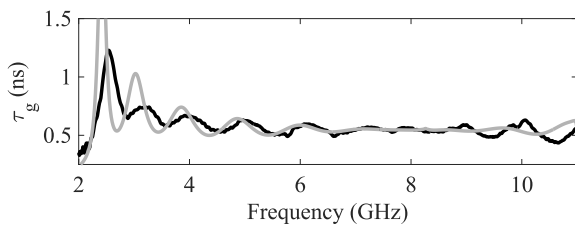

Fig. 17. Obtained τ_{g1} from measurements (black) and simulations (gray) for the DSRW with $l_1 = 4.0$ cm and TE_{10} mode excitation.
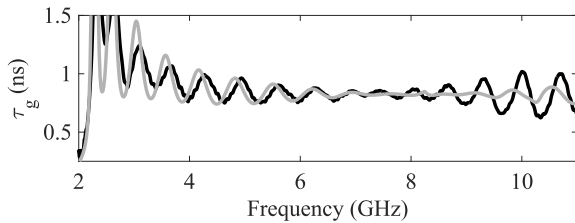

Fig. 18. Obtained τ_{g2} from measurements (black) and simulations (gray) for the DSRW with $l_2 = 7.0$ cm and TE_{10} mode excitation.

measured reflection coefficient is well below -15 dB for both the short and long DSRW sections, while transmission losses are -1.59 dB and -2.22 dB, respectively. At frequencies above 10 GHz, disagreement between simulations and measurements can be imputed to the TE_{40} mode appearance.

V. DSRW GROUP VELOCITY

The group delay was calculated using

$$\tau_g = -\frac{d\phi_{S_{21}}}{d\omega} \qquad (7)$$

for the two DSRW sections of lengths 4 and 7 cm, and for both the TE_{10} and TE_{20} feedings. Results obtained from simulations and measurements are given in Figs. 17 and 18 for the TE_{10} mode case. The fabricated proof of concept circuits

show a measured S-parameter behavior in good agreement with HFSS simulations. Around the design frequency of 7.95 GHz, the return losses are lower than -15 dB in all four cases, which ensures a correct calculation of the group delay using (7).
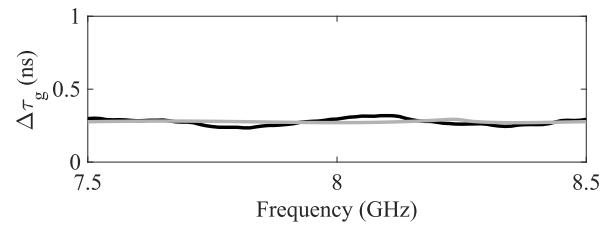

Fig. 19. DSRW obtained $\Delta\tau_g$ from measurements (black) and simulations (gray) for the TE_{10} mode excitation.
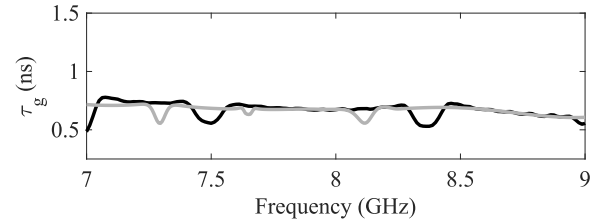

Fig. 20. Obtained τ_{g1} from measurements (black) and simulations (gray) for the DSRW with $l_1 = 4.0$ cm and TE_{20} mode excitation.
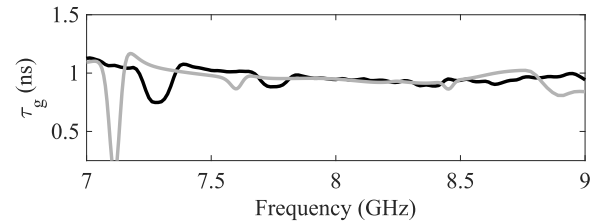

Fig. 21. Obtained τ_{g2} from measurements (black) and simulations (gray) for the DSRW with $l_2 = 7.0$ cm and TE_{20} mode excitation.

At the design frequency of 7.95 GHz, the measured group delay is 0.564 ns for the shorter section (Fig. 17) and 0.843 ns for the 7 cm long one (Fig. 18).

Finally, Fig. 19 shows the group delay difference $\Delta\tau_g$ between responses of Figs. 17 and 18 simulated and measured (for the TE_{10} mode) for a 1 GHz BW around the target frequency of 7.95 GHz. In that frequency range, both DSRW sections present a good reflection coefficient (see Figs. 11 and 12), guaranteeing that $\Delta\tau_g$ constitutes the group delay for a $l_2 - l_1 = 3.0$ cm long plain DSRW section (with no matching or feeding networks). At the design frequency, this measured difference is 0.28 ns, which implies a group velocity $v_g = 0.36c_0$ for the TE_{10} mode. For the TE_{20} mode excitation case, Figs. 20 and 21 show the group delay obtained from simulations and measurements.

Once more, it should be noted that, given the narrow BW behavior of the feeding networks used for exciting the TE_{20} mode, τ_g is only relevant around the target frequency of 7.95 GHz. At this frequency, the 4 cm long device gives a group delay of 0.675 ns, while the 7 cm long DSRW provides at the same frequency 0.956 ns (see Figs. 20 and 21, respectively). In these figures, it is possible to observe a 2.0% frequency shift in the responses which could be ascribed either to errors in the fabrication process or in the determination of the high permittivity value $\varepsilon_{rc} = 7.4$. Measured group delays in the TE_{20} case for the two different length DSRW sections are slightly bigger than those measured for the respective sections in the TE_{10} mode case. This is due to the fact that

This article has been accepted for inclusion in a future issue of this journal. Content is final as presented, with the exception of pagination.

TORREGROSA-PENALVA et al.: 3-D-PRINTED DIELECTRIC SLAB RECTANGULAR WAVEGUIDE

9

TABLE II
SOLUTIONS PROPOSED FOR EQUALIZING DISPERSION
MECHANISMS IN RF INTERCONNECTS

Ref.	$\Delta\tau_g'$	Scalable	Additional elements	Dispersion equalization
[15]	1	Yes	No	intermodal
[25]	0	Yes	Yes	inter/intramodal
This work	2.2	Yes	No	inter/intramodal
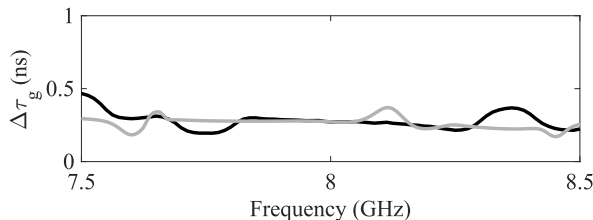
Fig. 22. DSRW calculated $\Delta\tau_g$ from measurements (black) and simulations (gray) for the TE_{20} mode excitation.

Fig. 23. Dispersion diagrams for the first two modes (TE_{10} and TE_{20}) propagating in the implemented DSRW obtained from S-parameter measurements (black line) and from theory (gray line).

Fig. 24. Left, dispersion diagrams for the first three modes (TE_{10}, TE_{20}, and TE_{30}) propagating in the CMOS technology DSRW example. Right, group velocity of the first three modes propagating in the structure.

input/output sections for feeding the TE_{20} mode to the DSRW constitute a larger electrical length than those for the TE_{10} mode.

Finally, Fig. 22 provides the difference $\Delta\tau_g$ between τ_{g2} and τ_{g1} of Figs. 21 and 20 which constitutes the group delay for the TE_{20} mode in a $l_2 - l_1 = 3.0$ cm long DSRW section. At the design frequency, the measured difference is, as expected, 0.28 ns, which implies a mode group velocity $v_g = 0.36c_0$. The waveguide dispersion can be characterized as the normalized variation of the group delay within a particular fractional bandwidth, $\Delta\tau_g' = (\frac{\Delta\tau_g}{\tau_g}/\frac{\Delta f}{f_0})$. This figure of merit is around 1 (depending on the bandwidth) when applied to the best intramodal dispersion compensation scheme of [15], while in our work, it yields 2.2 if the measured results given if Figs. 19 and 22 are considered. It should be noted that our result includes both intramodal and intermodal dispersion, and also that result from Smith and Abhari [15] is reached at the expense of including additional external devices to the transmission waveguide. Table II summarizes some of the characteristics of different solutions proposed for equalizing dispersion mechanisms in RF interconnects.

In order to further confirm the expected behavior of the implemented proof of concept DSRW, the dispersion diagrams for the TE_{10} and TE_{20} modes were extracted following the method described in Janezic and Jargon [28] from their respective measured S-parameters. They are shown in Fig. 23 compared to the theoretical dispersion diagrams of Fig. 2(j). Fig. 23 shows a remarkable agreement between the DSRW theoretical dispersion diagrams and the ones obtained from the proof of concept DSRW implementation measurements. This confirms the equalization BW targeted in this work and shown in Fig. 2(k). It is possible to confirm that around 7.95 GHz both dispersion diagram are parallel as expected.

VI. CHIP-TO-CHIP COMMUNICATIONS APPLICATION

As it has been pointed out in Section I, chip-to-chip interconnects have been devised in the low THz range by means of waveguide dev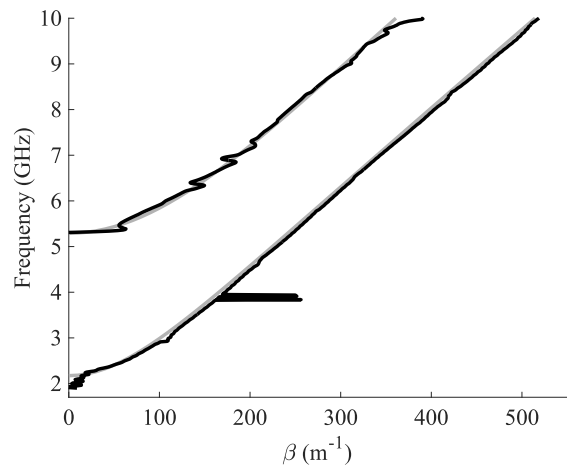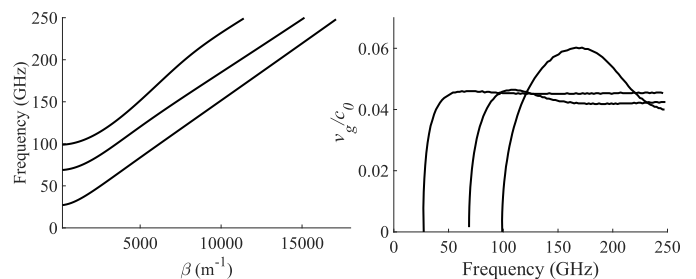ices [9]. The DSRW proposed in this work could be used in chip-to-chip communications by reproducing the study presented in Fig. 2 according to available material properties and to the desired communication frequency and BW interconnect. For instance, in CMOS technology, if silicon and silicon dioxide are used to implement the DSRW ($\varepsilon_{rc} = \varepsilon_{rSi} = 11.9$ and $\varepsilon_{rd} = \varepsilon_{rSiO_2} = 4$), the waveguide dimensions should be downscaled considerably to produce a proper interconnect in the low THz range. A similar study to the one presented in Fig. 2, would yield the DSRW structure of Fig. 1 with $a = 2$ mm and $c = 0.51$ mm to provide a waveguide interconnect were the three first propagating modes are equalized at 125 GHz. Fig. 24 shows the dispersion diagram of the first three modes propagating in such a DSRW as well as their group velocity. A transmission link using a carrier frequency of 125 GHz would experience no intermodal dispersion since all three modes propagating at that frequency exhibit the same group velocity. Additionally, HFSS simulations of a 10 mm long section of such a DSRW show insertion losses of -1.06 dB at 125 GHz in agreement with [9], (aluminum is used for metallic walls).

VII. CONCLUSION

This work presents for the first time, to the authors' knowledge, a proof of concept for equalizing the first two propagating modes in the DSRW. The suggested waveguide implementation, properly scaled, could be used in chip-to-chip interconnects to enhance the BW density while preserving

the integrity of the signals being transmitted. The proposed DSRW design exhibits a 45% equalization BW for a $\pm 2.5\%$ group velocity deviation range. Two sections with different lengths have been fabricated by means of AM techniques and two materials with different permittivity. These manufactured sections include feeding networks for exciting either the TE_{10} mode or the TE_{20} mode at a targeted frequency of 7.95 GHz. Theoretical and experimental results reveal that the designed DSRW yields, as expected, the same group velocity for the TE_{10} and the TE_{20} modes at that frequency. Moreover, *S*-parameter measurements have been employed to extract the dispersion diagram of the presented DSRW which agrees remarkably with theoretical predictions, demonstrating the desired mode equalization in the proposed waveguide implementation.

REFERENCES

[1] X. Zheng and A. V. Krishnamoorthy, "Si photonics technology for future optical interconnection," in *Proc. Asia Commun. Photon. Conf. Exhib. (ACP)*, Nov. 2011, pp. 1–11, doi: 10.1117/12.902258.

[2] Q. J. Gu, "THz interconnect: The last centimeter communication," *IEEE Commun. Mag.*, vol. 53, no. 4, pp. 206–215, Apr. 2015, doi: 10.1109/MCOM.2015.7081096.

[3] B. Yu, Y. Liu, Y. Ye, J. Ren, X. Liu, and Q. J. Gu, "High-efficiency micromachined sub-THz channels for low-cost interconnect for planar integrated circuits," *IEEE Trans. Microw. Theory Techn.*, vol. 64, no. 1, pp. 96–105, Jan. 2016, doi: 10.1109/TMTT.2015.2504443.

[4] B. Yu, Y. Ye, X. Ding, Y. Liu, X. Liu, and Q. J. Gu, "Dielectric waveguide based multi-mode sub-THz interconnect channel for high data-rate high bandwidth-density planar chip-to-chip communications," in *IEEE MTT-S Int. Microw. Symp. Dig.*, Jun. 2017, pp. 1750–1752, doi: 10.1109/MWSYM.2017.8058983.

[5] X.-D. Deng, Y. Li, W. Wu, and Y.-Z. Xiong, "A D-band chip-to-waveguide-horn (CWH) antenna with 18.9 dBi gain using CMOS technology," in *Proc. IEEE Int. Wireless Symp. (IWS)*, Mar. 2015, pp. 1–4, doi: 10.1109/IEEE-IWS.2015.7164518.

[6] L. Samoska et al., "A submillimeter-wave HEMT amplifier module with integrated waveguide transitions operating above 300 GHz," *IEEE Trans. Microw. Theory Techn.*, vol. 56, no. 6, pp. 1380–1388, Jun. 2008, doi: 10.1109/TMTT.2008.923353.

[7] D. L. Cuenca, J. Hesselbarth, and G. Alavi, "Low-loss mm-wave transition from on-chip microstrip to rectangular waveguide," in *Proc. 12th Eur. Microw. Integr. Circuits Conf. (EuMIC)*, Oct. 2017, pp. 325–328, doi: 10.23919/EuMIC.2017.8230724.

[8] N. Dolatsha, N. Saiz, and A. Arbabian, "Fully packaged millimetre-wave dielectric waveguide with multimodal excitation," *Electron. Lett.*, vol. 51, no. 17, pp. 1339–1341, Aug. 2015, doi: 10.1049/el.2015.2306.

[9] G. Gentile et al., "Silicon-filled rectangular waveguides and frequency scanning antennas for mm-wave integrated systems," *IEEE Trans. Antennas Propag.*, vol. 61, no. 12, pp. 5893–5901, Dec. 2013, doi: 10.1109/TAP.2013.2281518.

[10] J. W. Holloway, L. Boglione, T. M. Hancock, and R. Han, "A fully integrated broadband sub-mmWave chip-to-chip interconnect," *IEEE Trans. Microw. Theory Techn.*, vol. 65, no. 7, pp. 2373–2386, Jul. 2017, doi: 10.1109/TMTT.2017.2660491.

[11] B. Yu et al., "Ortho-mode sub-THz interconnect channel for planar chip-to-chip communications," *IEEE Trans. Microw. Theory Techn.*, vol. 66, no. 4, pp. 1864–1873, Apr. 2018, doi: 10.1109/TMTT.2017.2779496.

[12] N. Dolatsha, C. Chen, and A. Arbabian, "Loss and dispersion limitations in mm-wave dielectric waveguides for high-speed links," *IEEE Trans. THz Sci. Technol.*, vol. 6, no. 4, pp. 637–640, Jul. 2016, doi: 10.1109/TTHZ.2016.2574326.

[13] O. E. Mattia, M. Sawaby, K. Zheng, A. Arbabian, and B. Murmann, "A 10-Gbps continuous-time linear equalizer for mm-wave dielectric waveguide communication," *IEEE Solid-State Circuits Lett.*, vol. 3, pp. 266–269, 2020, doi: 10.1109/LSSC.2020.3014859.

[14] A. Suntives and R. Abhari, "Design and application of multimode substrate integrated waveguides in parallel multichannel signaling systems," *IEEE Trans. Microw. Theory Techn.*, vol. 57, no. 6, pp. 1563–1571, Jun. 2009, doi: 10.1109/TMTT.2009.2020777.

[15] N. A. Smith and R. Abhari, "Dispersion-equalization techniques for substrate integrated waveguide interconnects," *IEEE Trans. Microw. Theory Techn.*, vol. 58, no. 12, pp. 3824–3831, Dec. 2010, doi: 10.1109/TMTT.2010.2083911.

[16] N. Wang, X.-C. Li, and J.-F. Mao, "High-speed interconnect system using QPSK scheme based on substrate integrated waveguide," *J. Circuits, Syst. Comput.*, vol. 27, no. 1, 2018, Art. no. 1850014, doi: 10.1142/S0218126618500147.

[17] Y.-G. Nan, J. Pan, F. Liu, X. Hu, and P. Mégret, "Fiber Bragg grating spectra in graded-index multimode optical fibers," *J. Lightw. Technol.*, vol. 41, no. 13, pp. 4411–4418, Jul. 1, 2022, doi: 10.1109/JLT.2022.3228506.

[18] N. Shibata, K. Watanabe, and M. Ohashi, "Modal dispersion characteristics of LP0m modes in a step-index multimode fiber," *Appl. Opt.*, vol. 61, no. 31, pp. 9305–9310, 2022, doi: 10.1364/AO.471795.

[19] M. Van Den Hout et al., "1 Tbit/s/λ transmission over a 130 km link consisting of graded-index 50 μm core multi-mode fiber and 6LP few-mode fiber," in *Proc. 46th Eur. Conf. Optical Commun. (ECOC)*, 2020, pp. 1–4, doi: 10.1109/ECOC48923.2020.9333379.

[20] M. Atef, R. Swoboda, and H. Zimmermann, "1.25 Gbit/s over 50 m step-index plastic optical fiber using a fully integrated optical receiver with an integrated equalizer," *J. Lightw. Technol.*, vol. 30, no. 1, pp. 118–122, Jan. 2012, doi: 10.1109/JLT.2011.2179520.

[21] W. P. Ayres, P. H. Vartanian, and A. L. Helgesson, "Propagation in dielectric slab loaded rectangular waveguide," *IRE Trans. Microw. Theory Techn.*, vol. 6, no. 2, pp. 215–222, Apr. 1958, doi: 10.1109/TMTT.1958.1124541.

[22] E. Massoni et al., "3-D printed substrate integrated slab waveguide for single-mode bandwidth enhancement," *IEEE Microw. Wireless Compon. Lett.*, vol. 27, no. 6, pp. 536–538, Jun. 2017, doi: 10.1109/LMWC.2017.2701323.

[23] H. García-Martínez et al., "Design and fabrication of a band-pass filter with EBG single-ridge waveguide using additive manufacturing techniques," *IEEE Trans. Microw. Theory Techn.*, vol. 68, no. 10, pp. 4361–4368, Oct. 2020, doi: 10.1109/TMTT.2020.3006836.

[24] H. García-Martínez, G. Torregrosa-Penalva, E. Àvila-Navarro, N. Delmonte, L. Silvestri, and M. Bozzi, "3D-printed electromagnetic band-gap band-pass filter based on empty single-ridge waveguide," *IEEE Access*, vol. 10, pp. 53954–53962, 2022, doi: 10.1109/ACCESS.2022.3175868.

[25] A. Meyer, K. Krüger, and M. Schneider, "Dispersion-minimized rod and tube dielectric waveguides at *W*-band and *D*-band frequencies," *IEEE Microw. Wireless Compon. Lett.*, vol. 28, no. 7, pp. 555–557, Jul. 2018, doi: 10.1109/LMWC.2018.2839649.

[26] P. Wu, J. Liu, and Q. Xue, "Wideband excitation technology of TE_{20} mode substrate integrated waveguide (SIW) and its applications," *IEEE Trans. Microw. Theory Techn.*, vol. 63, no. 6, pp. 1863–1874, Jun. 2015, doi: 10.1109/TMTT.2015.2427808.

[27] G. Torregrosa-Penalva, H. García-Martínez, Á. E. Ortega-Argüello, A. Rodríguez-Martínez, A. Busqué-Nadal, and E. Ávila-Navarro, "Implementation of microwave circuits using stereolithography," *Polymers*, vol. 14, no. 8, p. 1612, Apr. 2022, doi: 10.3390/polym14081612.

[28] M. D. Janezic and J. A. Jargon, "Complex permittivity determination from propagation constant measurements," *IEEE Microw. Guided Wave Lett.*, vol. 9, no. 2, pp. 76–78, Feb. 1999, doi: 10.1109/75.755052.

Germán Torregrosa-Penalva was born in Novelda, Spain, in 1976. He received the Ph.D. degree in telecommunications engineering from the Universidad Politécnica de Madrid, Madrid, Spain, in 1999 and 2004, respectively.

In 2002, he joined the Miguel Hernández University of Elche (UMH), Elche, Spain, where he is currently an Associate Professor. Since 2023, he has been a part of Elche Microwave Laboratory (EMwLab), UMH. His current research activities include the conception and design of novel microwave circuits implemented with additive manufacturing techniques, the characterization of the dielectric properties of materials using high-frequency techniques and circuits, the design of microwave sensors for different applications, and the design of microwave circuits for educational and industrial purposes.

Héctor García-Martínez (Member, IEEE) was born in Albatera, Spain, in 1991. He received the M.S. degree in telecommunication engineering and the Ph.D. degree in industrial and telecommunication technologies from the Miguel Hernández University of Elche (UMH), Elche, Spain, in 2017 and 2021, respectively.

He was a Visiting Scholar with the Microwave Laboratory, University of Pavia, Pavia, Italy, in 2019. He is currently an Assistant Professor with the Department of Materials Science, Optics and Electronic Technology, and a member with the Elche Microwave Laboratory (EMwLab). His research interests include the design of passive and active microwave circuits in complex structures through 3-D additive manufacturing techniques and the analysis of biological materials using microwave devices.

Ernesto Ávila-Navarro was born in Elche, Spain, in 1974. He received the M.Sc. degree in telecommunication engineering from the Polytechnic University of Valencia, Valencia, Spain, in 1998, and the Ph.D. degree from the Miguel Hernández University of Elche, Elche, in 2008, with a doctoral thesis in printed antennas.

In 2000, he joined the University Miguel Hernández of Elche, Elche, where he is an Associate Professor with the Department of Materials Science, Optics and Electronic Technology, and a Researcher of the Microwave Laboratory of Elche (EMwLab), Elche. His current research interests include printed antennas, passive and active microwave devices, bioelectronics, and dielectric characterization of materials at microwave frequencies and microwave imaging systems for tumor detection.

Paula Viudes-Pérez was born in Elche, Spain, in 1999. She received the master's degree in telecommunications engineering from Miguel Hernández University of Elche (UMH), Elche, in 2024, where she is currently pursuing the Ph.D. degree in industrial and telecommunications technologies.

She is currently a Predoctoral Researcher with Elche Microwave Laboratory (EMwLab), UMH. Her research interests include the implementation of novel microwave devices by using additive manufacturing techniques, the design of microwave sensors, and the dielectric characterization of materials using microwave frequencies.

Maurizio Bozzi (Fellow, IEEE) received the Ph.D. degree in electronics and computer science from the University of Pavia, Pavia, Italy, in 2000.

He held research positions with various universities worldwide, including the Technische Universitaet Darmstadt, Darmstadt, Germany; the Universitat de Valencia, Valencia, Spain; and the Ecole Polytechnique de Montreal, Montreal, QC, Canada. In 2002, he joined with the Department of Electronics, University of Pavia, where he is currently a Full Professor of electromagnetic fields. He was also a Guest Professor with Tianjin University, Tianjin, China, from 2015 to 2017 and a Visiting Professor with Gdansk University of Technology, Gdańsk, Poland, from 2017 to 2018. He has authored or coauthored more than 180 journal articles and 360 conference papers. He co-edited the book *Periodic Structures* (Research Signpost, 2006) and coauthored the book *Microstrip Lines and Slotlines* (Artech House, 2013). His main research interests concern the computational electromagnetics, the substrate integrated waveguide technology, and the use of novel materials and fabrication technologies for microwave circuits (including paper, textile, and 3-D printing).

Prof. Bozzi was a member of the General Assembly of the European Microwave Association (EuMA) from 2014 to 2016. He is the 2024 President of the IEEE Microwave Theory and Technology Society (MTT-S). He was an Elected Member of the Administrative Committee of MTT-S for years 2017 to 2022, the Budget Committee Chair in 2023, the MTT-S Treasurer from 2020 to 2022, the Chair of the Meetings and Symposia Committee for years 2018 and 2019, and the Secretary of MTT-S in 2016. He was the General Chair of the IEEE MTT-S International Microwave Workshop Series-Advanced Materials and Processes (IMWS-AMP 2017), in Pavia, 2017, of the inaugural edition of the IEEE International Conference on Numerical Electromagnetic Modeling and Optimization (NEMO2014), in Pavia, 2014, and of the IEEE MTT-S International Microwave Workshop Series on Millimeter Wave Integration Technologies, in Sitges, Spain, 2011. He received several awards, including the 2015 Premium Award for Best Paper in IET Microwaves, Antennas and Propagation, the 2014 Premium Award for the Best Paper in Electronics Letters, the Best Student Paper Award at the 2016 IEEE Topical Conference on Wireless Sensors and Sensor Networks (WiSNet2016), the Best Paper Award at the 15th Mediterranean Microwave Symposium (MMS2015), the Best Student Award at the 4th European Conference on Antennas and Propagation (EuCAP 2010), the Best Young Scientist Paper Award of the XXVII General Assembly of URSI in 2002, and the MECSA Prize of the Italian Conference on Electromagnetics (XIII RiNEm) in 2000. He was a Track Editor of IEEE TRANSACTIONS ON MICROWAVE THEORY AND TECHNIQUES, and an Associate Editor of IEEE MICROWAVE AND WIRELESS COMPONENTS LETTERS, *IET Microwaves, Antennas and Propagation*, and *IET Electronics Letters*.

Enrique Bronchalo was born Guadalajara, Spain, in 1963. He received the bachelor's degree from the Complutense University of Madrid, Madrid, Spain, in 1986, and the Ph.D. degree in physics from the Alcalá University, Alcalá de Henares, Spain, in 1996.

In 2001, he joined the Miguel Hernández University, Elche, Spain, where he holds an Associate Professor position with the Signal Theory and Communications Division. His current research interests include the passive microwave devices and microwave sensors.